Lattice Boltzmann method on a curvilinear coordinate system: Vortex shedding behind a circular cylinder

Xiaoyi He[1,2] and Gary D. Doolen[2]

[1]*Center for Nonlinear Studies, MS-B258, Los Alamos National Laboratory, Los Alamos, New Mexico 87545*
[2]*Complex Systems, Group T-13, MS-B213, Theoretical Division, Los Alamos National Laboratory, Los Alamos, New Mexico 87545*

The interpolation-supplemented lattice Boltzmann equation (ISLBE) method is used to simulate the two-dimensional vortex shedding behind a circular cylinder at low Reynolds numbers. Simulations are carried out on a polar-coordinate grid system with a dense grid distributed near the cylinder surface. The Strouhal number, the drag, and the lift coefficients obtained from the simulations agree well with previous experimental measurements and classical computational fluid dynamics simulations. Comparisons of detailed flow patterns with other studies via streamlines and streaklines are also satisfactory. The ability of the ISLBE scheme to simulate complicated long-term periodic flow phenomena is demonstrated.
[S1063-651X(97)00507-2]

I. INTRODUCTION

The lattice Boltzmann equation (LBE) method has been proposed as a useful computational fluid dynamics approaches for simulations of complex flows [1,2]. Although the lattice Boltzmann equation itself has long been proved to recover the Navier-Stokes equation through the Chapman-Enskog expansion [3,4], the LBE method has not been widely accepted by the engineering community as a practical computational fluid dynamics (CFD) tool. One reason for this is the restriction of previous LBE models to the regular lattices [5]. For many practical problems, a variable computational mesh is always desired. There has been much activity in recent years to construct LBE schemes that can be implemented on a variable computational grid [6–8]. One of these models, which will be specifically addressed in this paper, is the interpolation-supplemented lattice Boltzmann equation (ISLBE) scheme [7].

The restriction of the previous LBE models to regular lattices has historical roots. This aspect is directly inherited from the lattice-gas automaton (LGA) [9,10], the precursor of the LBE method. In the LGA, the time evolution of a flow system is simulated by tracking the microscopic movements of constituent particles hopping between the sites of a regular lattice. A regular lattice is essential for the LGA since the particle population in the LGA is a Boolean type and the particle collision must take place at lattice sites. This restriction, however, becomes redundant in the LBE method because a real-number single-particle distribution is used in the LBE method to replace the Boolean particle population in the LGA [7,8]. With a real-number representation, the single-particle distribution can be regarded as a continuous function in the physical space and its value can be determined at any location in the computational domain.

In the ISLBE scheme, a flow domain is discretized into an arbitrary grid mesh. At each grid node sits a regular velocity lattice. The ISLBE scheme consists of three steps: relaxation, advection, and interpolation. The first two steps are exactly the same as those of the previous LBE models: the distribu-

tion function first relaxes to the local equilibrium distribution and then freely advects at the corresponding velocity. The interpolation step, which does not exist in the previous LBE models, is introduced to reconstruct the distribution function at grid nodes at the next time step. The interpolation scheme must have at least a second-order accuracy to avoid destructive numerical diffusivity and viscosity [11].

The ISLBE scheme was applied to a nonuniform rectangular mesh in [7]. In this reference, numerical simulations of steady flow in a sudden expansion channel yielded satisfactory results. More convincing evidence comes from a later study on flow around an impulsively started circular cylinder in which a polar coordinate grid system was used [12]. In that study, the ISLBE simulation successfully reproduced the entire process of wake formation for Reynolds numbers ranging from 10 to 40. Characteristic steady-state parameters, including wake length, separation angle, drag coefficients, and stagnation pressure coefficients, agree well with previous experimental measurements and traditional CFD simulations. For moderate and high Reynolds numbers ($300 < \text{Re} < 9600$), the ISLBE scheme was also able to simulate correctly the initial stage of the flow development. Flow features in this regime, such as the secondary vortex and the ''forewake,'' were reproduced in ISLBE simulations [12]. Nevertheless, there is another type of flow that is practically important but was neglected in previous ISLBE studies. That is the long-term unsteady flow phenomenon such as the periodic vortex shedding behind a circular cylinder.

An understanding of the vortex shedding process behind a circular cylinder poses a challenge to both basic research and general applications. There are many studies on this topic in the literature, including those using the lattice Boltzmann equation method [13–15]. Excellent reviews have been given by Berger and Wille [16] and recently by Williamson [17]. It is generally agreed that in two dimensions the vortex shedding begins at a critical Reynolds number around 49 [17]. Here the Reynolds number is defined as $\text{Re} = 2Ua/\nu$, where U is the far-field flow velocity, a is the radius of the cylinder, and ν is the viscosity. Above this critical Reynolds

number, vorticity is shed downstream from alternate sides of the cylinder, forming a von Kármán vortex street. The Strouhal number ($S = fD/U$, where f is the shedding frequency) strongly depends on the Reynolds number. At low Reynolds numbers, the flow field is two dimensional. When the Reynolds number increases to a second critical value around 140–194, three-dimensional structure of the flow field becomes essential (see, e.g., [17]).

This study will only focus on the two-dimensional (2D) vortex shedding behind a circular cylinder. For this reason, the Reynolds numbers in the simulation are chosen to be 50, 100, and 150. The Strouhal number, the drag, and the lift coefficients will be compared with previous experimental measurements and numerical simulations. In addition, the detailed flow pattern will be extensively analyzed using both streamlines and streaklines. The rest of this paper is organized as follows. Section II introduces the ISLBE scheme. The mesh setup, boundary condition, and initial condition are also described in this section. Section III presents the results of numerical simulations and compares them with previous studies. Section IV discusses the results and concludes the paper.

II. NUMERICAL METHOD

Since the numerical method used in this study has been described elsewhere [12], only an outline is given here. The computational domain consists of a circular region of a large but finite radius outside a 2D circular cylinder. This domain is covered with a polar coordinate grid (Fig. 1). The coordinates of the grid nodes are

$$r_i = a e^{\pi \xi_i}, \quad \theta_j = \pi \eta_j, \tag{1}$$

where

$$\xi_i = \xi_\infty \frac{i-1}{NX-1}, \quad i = 1, 2, \ldots, NX$$

$$\eta_j = 2 \frac{j-1}{NY-1} - 1, \quad j = 1, 2, \ldots, NY. \tag{2}$$

The logarithmic transformation of the radial coordinate is selected because it provides a dense grid near the cylinder where the largest gradients occur.
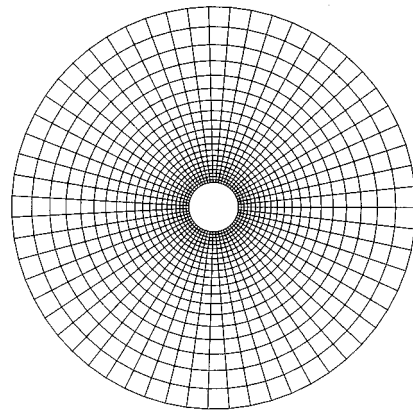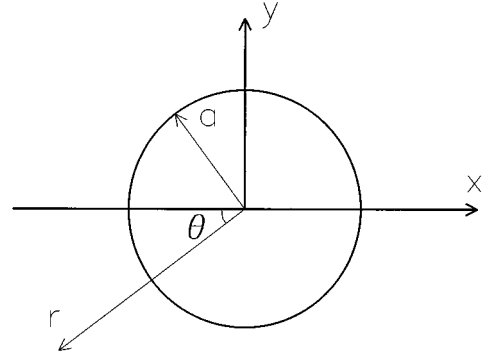

FIG. 1. Polar coordinate system and computational mesh ($NX \times NY = 21 \times 61$ and $\xi_\infty = 2/3$ as an example).

The ISLBE scheme consists of three steps: relaxation, advection, and interpolation. The first two steps are exactly the same as those in previous LBE models, i.e., the distribution function is updated each time step using the lattice Boltzmann equation

$$p_\alpha(\mathbf{x} + \mathbf{e}_\alpha \delta_t, t + \delta_t) - p_\alpha(\mathbf{x}, t) = \frac{1}{\tau}[g_\alpha(\mathbf{x}t) - p_\alpha(\mathbf{x}, t)], \tag{3}$$

where p_α is the pressure distribution and g_α is its corresponding equilibrium state. Here the nine-bit incompressible lattice Boltzmann BGK model [18] is used. The nine discrete velocities $\mathbf{e}_\alpha$ are defined by

$$\mathbf{e}_\alpha = \begin{cases} \mathbf{0}, & \alpha = 0 \\ (\cos[(\alpha-1)\pi/2], \sin[(\alpha-1)\pi/2])c, & \alpha = 1, \ldots, 4 \\ \sqrt{2}(\cos[(\alpha-5)\pi/2 + \pi/4], \sin[(\alpha-5)\pi/2 + \pi/4])c, & \alpha = 5, \ldots, 8. \end{cases} \tag{4}$$

The parameters c and δ_t are the advection speed and time step, respectively. τ is the dimensionless relaxation time, which is related to the fluid viscosity by

$$\nu = \frac{2\tau - 1}{6} c^2 \delta_t .$$

The equilibrium pressure distribution g_α is chosen to be

$$g_\alpha = w_\alpha \left[p + \rho \left((\mathbf{e}_\alpha \cdot \mathbf{u}) + \frac{3}{2} \frac{(\mathbf{e}_\alpha \cdot \mathbf{u})^2}{c^2} - \frac{1}{2} \mathbf{u}^2 \right) \right], \quad (5)$$

with $w_0 = 4/9$, $w_\alpha = 1/9$ for $\alpha = 1, \ldots, 4$, and $w_\alpha = 1/36$ for $\alpha = 5, \ldots, 8$. The density ρ is constant in incompressible flows. The macroscopic pressure p and the velocity $\mathbf{u}$ are calculated using

$$p = \sum_\alpha p_\alpha, \quad (6)$$

$$\mathbf{u} = \frac{1}{\rho c_s^2} \sum_\alpha \mathbf{e}_\alpha p_\alpha, \quad (7)$$

where $c_s = c/\sqrt{3}$ is the sound speed.

According to Eq. (3), the distribution function at the next time step is exactly known only at $\mathbf{x}_{i,j} + \mathbf{e}_\alpha \delta_t$, where $\mathbf{x}_{i,j}$'s are the grid nodes. An interpolation step is necessary to reconstruct the post-advection distribution at each grid node. Notice that, for each $\mathbf{e}_\alpha$, the shifted computational domain

FIG. 2. Time evolution of the drag and lift coefficients for Re = 100. Time is in units of a/U.

$\mathbf{x} + \mathbf{e}_\alpha \delta_t$ can be described by the same polar coordinate grid. To reconstruct the distribution, it is convenient to calculate the displacement from the original grid node

$$d\xi_i = \xi(\mathbf{x} - \mathbf{e}_\alpha \delta_t) - \xi_i,$$

$$d\eta_j = \eta(\mathbf{x} - \mathbf{e}_\alpha \delta_t) - \eta_j .$$

Once the displacement is known, the post-advection distribution at the original grid node can be calculated using a second-order upwind interpolation scheme

$$p_\alpha(\mathbf{x}_{i,j}, t + \delta_t) = \sum_{k=0}^{2} \sum_{l=0}^{2} a_{i,k} b_{j,l} p_\alpha(r_{i+k\times i_d}, \theta_{j+l\times j_d}, t + \delta_t), \quad (8)$$

where $i_d = \text{sgn}(1, d\xi_i)$ and $j_d = \text{sgn}(1, d\eta_j)$ determine the upwind direction. The interpolation coefficients in Eq. (8) are calculated using

$$a_{i,0} = \frac{(|d\xi_i| - \Delta\xi)(|d\xi_i| - 2\Delta\xi)}{2\Delta\xi^2},$$

$$b_{j,0} = \frac{(|d\eta_j| - \Delta\eta)(|d\eta_j| - 2\Delta\eta)}{2\Delta\eta^2},$$

$$a_{i,1} = -\frac{|d\xi_i|(|d\xi_i| - 2\Delta\xi)}{\Delta\xi^2}, \quad b_{j,1} = -\frac{|d\eta_j|(|d\eta_j| - 2\Delta\eta)}{\Delta\eta^2}, \quad (9)$$

$$a_{i,2} = \frac{|d\xi_i|(|d\xi_i| - \Delta\xi)}{2\Delta\xi^2}, \quad b_{j,2} = \frac{|d\eta_j|(|d\eta_j| - \Delta\eta)}{2\Delta\eta^2},$$

where $\Delta\xi = \xi_\infty/(NX - 1)$ and $\Delta\eta = 2/(NY - 1)$.

The nonslip boundary condition is applied at the cylinder wall. This study implements the nonslip condition using the bounce-back rule. In the bounce-back rule, particles colliding with a wall simply reverse their velocities. Notice that the bounce-back rule yields an effective wall halfway between the bounce-back row and its adjacent row in the fluid [19]. This effect should be taken into account in calculating the viscous stress on the cylinder.
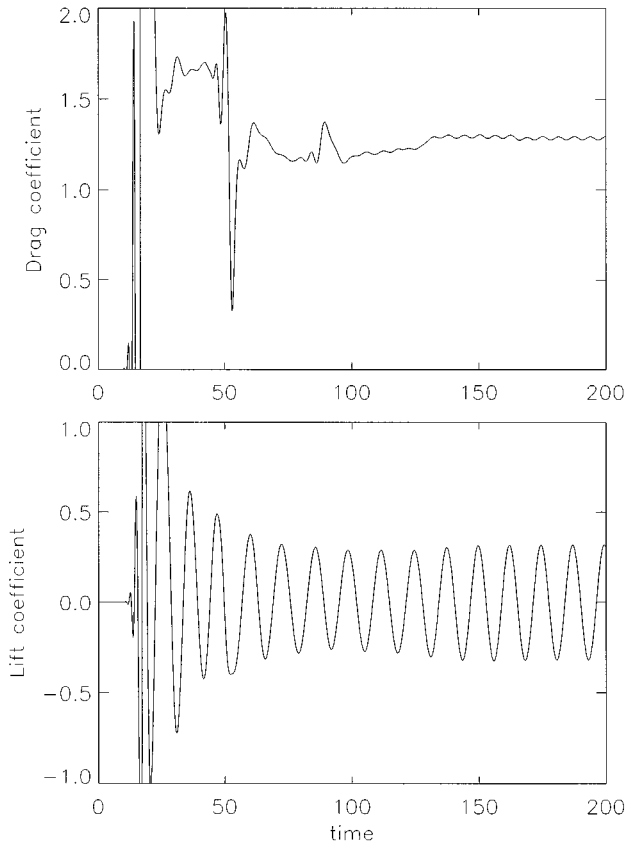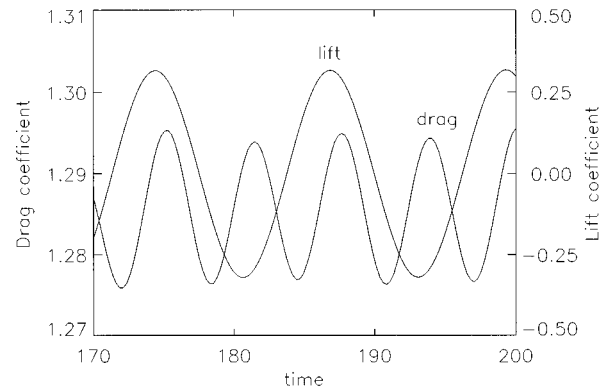

FIG. 3. Comparison of the oscillatory drag and lift coefficients in the final stage. Time is measured from the beginning of the simulation.

TABLE I. Comparison of the calculated and measured Strouhal numbers.

Work	Re = 50	Re = 100	Re = 150
Ref. [16]	0.12–0.13	0.16–0.17	0.18–0.19
Ref. [20]	0.12	0.16	0.18
Ref. [21]	0.123	0.164	0.183
Ref. [22]	0.105	0.159	0.176
present	0.121	0.161	0.179

It is natural and computationally convenient to assume a potential flow at the outer boundary. With the far-field velocity and pressure known, the distribution function can be chosen to be the equilibrium state. In this study, the far-field velocity U is set to 0.1 and the far-field pressure p_∞ is set to 1/3.

Initially, the numerical simulation starts from an unsymmetric flow field

$$u_x = U\frac{ay}{r^2}, \quad u_y = -U\frac{ax}{r^2}. \tag{10}$$

This unsymmetric flow field serves as an artificial initiator for the vortex shedding process. For Reynolds numbers less than the critical value ($Re_{crt} \approx 49$), this asymmetry is gradually dissipated by viscosity (data not shown). For the Reynolds numbers chosen in this study ($Re > Re_{crt}$), the flow field eventually settles into a periodic oscillatory pattern.

III. RESULTS

The numerical simulations of the vortex shedding behind a circular cylinder were carried out for Reynolds numbers of 50, 100, and 150. Unless otherwise stated, all the reported data are obtained on a 181×241 grid. The outer boundary is located at $\xi_\infty = 1.5$ or $r_\infty/a = 111.3$. The time step, in units of a/U, is equal to 0.0025. The CPU time for each time step requires 0.2 s on an IBM-RISC 6000 workstation with a peak performance of 267×10^6 flops.

TABLE II. Comparisons of the drag and lift coefficients. $\overline{C}_D$, average drag coefficient; ΔC_D, drag oscillation (peak to peak); ΔC_L, lift oscillation (peak to peak).

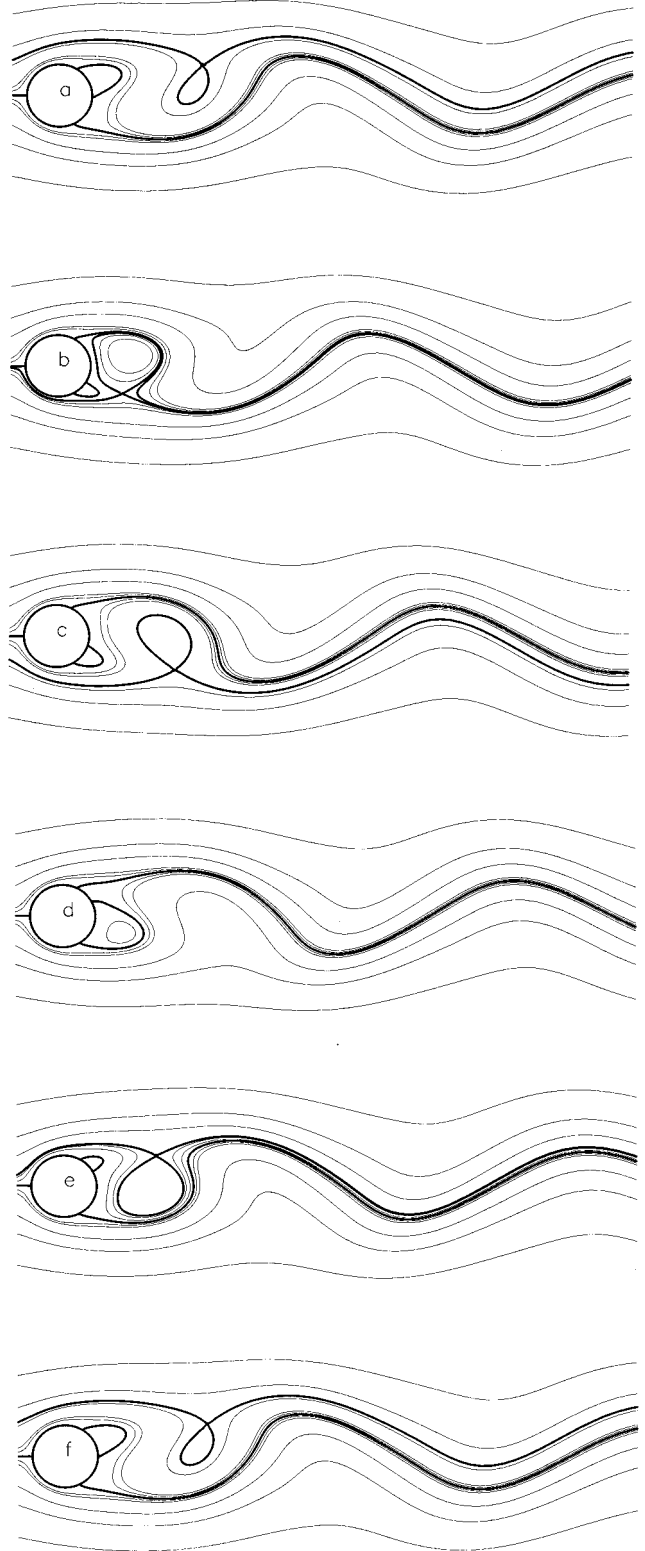| Re	Work	$\overline{C}_D$	ΔC_D	ΔC_L
50	Ref. [25]	1.40		
	Ref. [26]	1.45		
	present	1.394	0.002	0.11
100	Ref. [25]	1.25		
	Ref. [27]	1.28	0.012	0.54
	Ref. [28]	1.28	0.03	0.60
	Ref. [26]	1.35		
	present	1.287	0.018	0.64
150	Ref. [26]	1.33		
	present	1.261	0.048	0.98

FIG. 4. Sequence of streamlines in a complete shedding cycle, separated by intervals of $T/5$ (Re=100).

A. Vortex shedding and Strouhal number

The most attractive feature of the vortex shedding behind a circular cylinder is the periodic variation of the flow field. This periodicity has been successfully reproduced in this study. The periodic variation of the flow field can be illus-

trated by the time evolution of two characteristic parameters, the drag and lift coefficients, defined as

$$C_D = \frac{\mathbf{F} \cdot \mathbf{x}}{\rho U^2 a}, \quad C_L = \frac{\mathbf{F} \cdot \mathbf{y}}{\rho U^2 a}.$$

The total force acting on the circular cylinder $\mathbf{F}$, arises from the surface pressure and shear stress. It can be calculated using

$$\mathbf{F} = \int \mathbf{S} \cdot \mathbf{n} \, dl.$$

The integral is taken over the cylinder surface, $\mathbf{n}$ is the normal direction of the cylinder wall, and

$$\mathbf{S} = -p\mathbf{I} + \rho\nu(\nabla\mathbf{u} + \mathbf{u}\nabla)$$

is the stress tensor.

As shown in Fig. 2, the drag and lift coefficients varied irregularly at the beginning of each simulation due to the initial disturbance. After a certain time, these coefficients gradually evolved to periodic oscillations. The lift coefficient oscillated much more strongly than the drag coefficient. More detail about the final periodic state is shown in Fig. 3. The drag coefficient varies twice as fast as the lift coefficient as observed in previous studies [27,28]. This is because the drag coefficient is affected by vortex shedding processes from both sides of the cylinder.

The vortex shedding frequency can be obtained by measuring the final period of the lift coefficient. The calculated Strouhal numbers are listed in Table I for Reynolds numbers of 50, 100, and 150, along with some previous experimental measurements. There once was considerable discussion on what factors affect the St-Re number relationship [23,24]. It is now generally believed that a universal St-Re curve exists for parallel vortex shedding [17]. The Strouhal numbers obtained in this study agree very well with the experimental measurements.

The average values and oscillations (peak to peak) of the drag and lift coefficients are listed in Table II. Also included are results from previous experimental measurements and numerical simulations. For all the Reynolds numbers simulated, agreement between the present and previous studies is satisfactory for the average drag coefficients. Our average drag coefficients are consistently smaller than the computational results of Henderson [26], but they are close to those reported by other authors. Comparisons of oscillations of the drag and lift coefficients are less satisfactory, but all the data are of the same order. Because the existing data for the oscillations of the drag and lift coefficients are rare, the reliability of our results can only be justified by future studies.

B. Streamlines

The global view of the vortex shedding process can be well illustrated using streamline plots. Since the flow patterns are similar for all the Reynolds numbers simulated, only the result for the Reynolds number of 100 will be presented. Following Perry *et al.* [29] and Eaton [30], we use some special terms in describing the streamline patterns. These special terms include centers, which are points surrounded by closed streamlines; saddles, which are points where a streamline crosses itself; and separatrices, which are streamlines that contain a saddle points.

Figure 4 shows the time evolution of vortex shedding over a complete cycle using a sequence of streamlines separated by intervals of $T/5$, where T is the period of the shedding cycle. Thick lines are used to distinguish the separatrices from ordinary streamlines. At the beginning of the shedding cycle [Fig. 4(a)], a large recirculation zone attached to the top of the cylinder and a vortex shed in the last cycle from the bottom of the cylinder was still visible. One-fifth of the period later [Fig. 4(b)], the recirculation zone at the top had broken off from the cylinder wall to form a new vortex, while another recirculation zone appeared at the bottom of the cylinder. The newly shed vortex gradually lost its strength as it traveled downstream [Fig. 4(c)], and disappeared before another recirculation zone was generated at the top of the cylinder [Fig. 4(d)]. In the meantime, the recirculation zone at the bottom of the cylinder gradually gained strength and then broke off into the wake to complete a shedding cycle [Figs. 4(e) and 4(f)].

The flow patterns in Fig. 4 are very similar to the experimental observations by Perry *et al.* [29] and the numerical simulations by Eaton [30]. One of the salient features in these streamline plots is the instant ''alleyways'' between two separatrices. Through these alleyways, fluid passing the cylinder surface flows up and down to move around the shed vortices and finally reaches the main stream. However, our
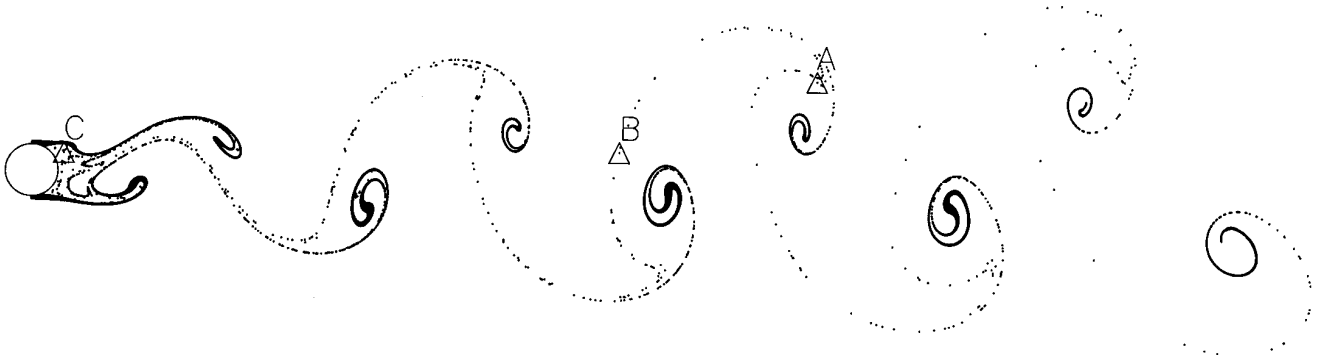

FIG. 5. von Kármán vortex street behind a circular cylinder using the ISLBE simulation (Re=100).

results did not show the coexistence of centers and saddles of two shed vortices as suggested by Perry *et al.* This observation is consistent with Eaton's numerical simulation.

The separation angles in our simulations were also found to oscillate at the shedding frequency. For the Reynolds number of 100, our simulation gives an average separation angle of $61°$ with an oscillation amplitude of $3°$. These data agree with the numerical results of $63° \pm 3°$ by Jordan and Fromm [27], $64° \pm 3°$ by Patel [31], and $63.5° \pm 3.5°$ by Braza *et al.* [28]. It is not clear why our separation angle is slightly smaller than those in previous studies. For other two Reynolds numbers, our simulations yield a separation angle of $55° \pm 0.5°$ for Re=50 and $63° \pm 5°$ for Re=150.

C. Streaklines

Although the instantaneous streamlines provide valuable information on variations of flow fields in vortex shedding, they do not give a clear picture of the vortex formation process. This is why the streakline technique (e.g., dye visualization) has been extensively used in many experiments. To demonstrate the ability of the ISLBE scheme to simulate the vortex shedding process, this section presents streaklines generated from the ISLBE simulation for the Reynolds number of 100 and compares them with previous experimental observations and numerical simulations.

The streaklines can be calculated by numerically integrating the equation

$$\frac{d\mathbf{x}}{dt} = \mathbf{u}(\mathbf{x}), \qquad (11)$$

where $\mathbf{x}$ is particle coordinates in streaklines and $\mathbf{u}$ is the local velocity. Figure 5 shows a typical von Kármán vortex street obtained by an ISLBE simulation. A total of ten streaklines were generated by releasing trace particles in intervals of $0.025a/U$. Five streaklines originate from 0.01, 0.02, 0.03, 0.04, and 0.05 diameters above the top of the cylinder, respectively, while the others start from the same distances below the bottom of the cylinder. The flow pattern is strikingly similar to the experimental observation by Taneda using a dye visualization technique [32].

It is important to notice the nonuniform movements of the trace particles in Fig. 5. Markers *A*, *B*, and *C* denote three trace particles released consecutively from the same location (0.05 diameter above the top of the cylinder). Although the initial distance between them was only $0.025a$, they deviated from each other by quite a distance after several shedding cycles. Most of the trace particles aggregate into the cores of the von Kármán vortices, while the rest of them are significantly stretched to form the delicate filaments connecting two consecutive vortex cores. The approach of particles from the opposite sides of the cylinder is quite clear. This result is consistent with the "fingering" or "multiple-folding" phenomenon observed by Gerrard [20] and Perry *et al.* [29].

To better illustrate the evolution of the streaklines, we connected the trace particles by lines to generate continuous streaklines. To avoid discontinuities, new trace particles are inserted wherever a streakline segment is severely stretched. Figure 6 shows a sequence of streaklines over a shedding cycle, separated by intervals of $T/5$. The times represented
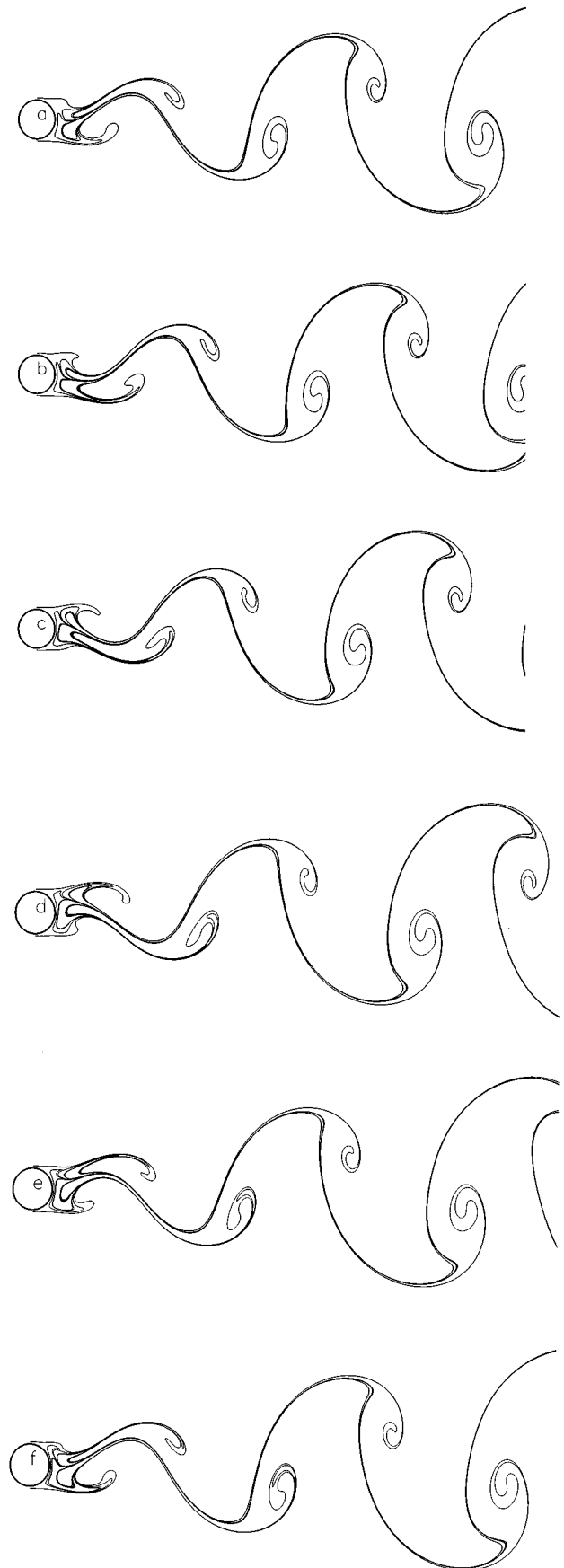

FIG. 6. Sequence of streaklines in a complete shedding cycle, separated by intervals of $T/5$ (Re=100).

here correspond exactly to those at which the streamlines were presented in Fig. 4. For clarity, only two streaklines on each side (0.05 diameter away from the cylinder wall) are plotted. Figure 6 clearly shows how vortices are generated over a shedding cycle. Near the top of the cylinder, the fluid just passing the cylinder travels rapidly and in a relative straight path. Since the fluids in the near wake move downward in the first half of the shedding cycle [see Figs. 4(a)–4(c)], the streaklines are pulled apart to form a small fold [Fig. 6(a)]. This fold gradually extrudes into the wake to generate an antennalike structure [Figs. 6(b) and 6(c)]. In the meantime, the ''antenna'' was rotated clockwise by the shear stress and gradually grew into a von Kármán vortex core. The same process occurs at the bottom of the cylinder in the second half of the shedding cycle [Figs. 6(d)–6(f)]. A counterclockwise vortex is shed into the wake from the bottom of the cylinder.

The streakline pattern in Fig. 6 is very much like the ''threading diagram'' proposed by Perry *et al.* [29] except for one important difference. In the threading diagram by Perry *et al.*, ''threads'' are pulled back from the downstream vortices and end in the near wake. The present result shows that some of these threads fold again and extrude into the downstream vortices. Because of these extruding threads, each von Kármán vortex contains multiple layers of streaklines. Each of these layers is composed of particles released in different cycles. Particles in the inner most layer are those released earliest. In the near wake, fluids are continuously squeezed out along with the extruding threads. However, there are always some fluids remaining in the wake because the proximal ends of the streaklines move very little over cycles. The extensive mixing behind the cylinder is obvious.

IV. CONCLUSION

The interpolation-supplemented lattice Boltzmann equation scheme was successfully applied to simulate the 2D vortex shedding phenomenon behind a circular cylinder for Reynolds numbers ranging from 50 to 150. The simulations are carried out on a polar coordinate grid with a dense grid distribution near the cylinder wall. The Strouhal numbers, the drag, and the lift coefficients are found to be in good agreement with previous experimental measurements and classical CFD studies. The detailed flow patterns are also consistent with previous experimental observations and numerical simulations. The instant alleyways of the streamlines and the multiple foldings of the streaklines are successfully reproduced in simulations.

The success of this study shows that the ISLBE scheme can be used as a versatile CFD tool with the ability to simulate complicated flows. With the ISLBE scheme, the restriction to regular lattices of previous LBE models is no longer necessary and a variable grid can be used as desired. Although previous studies [7,12] have shown the accuracy of the ISLBE scheme in simulation of steady or short-term unsteady flows, this study demonstrates the ability of the ISLBE scheme to simulate long-term unsteady flows.

[1] G. McNamara and G. Zanetti, Phys. Rev. Lett. **61**, 2332 (1988).

[2] F. J. Higuera and J. Jeménez, Europhys. Lett. **9**, 663 (1989).

[3] H. Chen, S. Chen, and W. H. Matthaeus, Phys. Rev. A **45**, R5339 (1991).

[4] Y. H. Qian, D. d'Humières, and P. Lallemand, Europhys. Lett. **17**, 479 (1992).

[5] S. Succi, G. Amati, and R. Benzi, J. Stat. Phys. **81**, 5 (1995).

[6] F. Nannelli and S. Succi, J. Stat. Phys. **68**, 401 (1992).

[7] X. He, L. S. Luo, and M. Dembo, J. Comput. Phys. **129**, 357 (1996).

[8] N. Cao *et al.*, Phys. Rev. E **55**, R21 (1997).

[9] S. Wolfram, J. Stat. Phys. **45**, 471 (1986).

[10] U. Frisch, B. Hasslacher, and Y. Pomeau, Phys. Rev. Lett. **56**, 1505 (1986).

[11] X. He, Int. J. Mod. Phys. C (to be published).

[12] X. He and G. Doolen, J. Comput. Phys. (to be published).

[13] L. Wagner, Phys. Rev. E **49**, 2115 (1994).

[14] L. Wagner, Phys. Fluids **6**, 3516 (1994).

[15] L. Wagner and F. Hayot, J. Stat. Phys. **81**, 63 (1995).

[16] E. Berger and R. Wille, Annu. Rev. Fluid Mech. **4**, 313 (1972).

[17] C. H. K. Williamson, Annu. Rev. Fluid Mech. **23**, 477 (1996).

[18] X. He and L. S. Luo, J. Stat. Phys. (to be published).

[19] I. Ginzbourg and P. M. Adler, J. Phys. (France) II **4**, 191 (1994).

[20] J. H. Gerrard, Philos. Trans. R. Soc. London, Ser. A **288**, 351 (1978).

[21] C. H. K. Williamson, Phys. Fluids **31**, 2742 (1988).

[22] M. Hammache and M. Gharib, Phys. Fluids A **1**, 1611 (1989).

[23] D. J. Tritton, J. Fluid Mech. **45**, 203 (1971).

[24] M. G. Gaster, J. Fluid Mech. **46**, 749 (1971).

[25] D. J. Tritton, J. Fluid Mech. **6**, 547 (1959).

[26] R. D. Henderson, Phys. Fluids **7**, 2102 (1995).

[27] S. Jordan and J. E. Fromm, Phys. Fluids **15**, 371 (1972).

[28] M. Braza, P. Chassaing, and H. Ha Minh, J. Fluid Mech. **165**, 79 (1986).

[29] A. E. Perry, M. S. Chong, and T. T. Lim, J. Fluid Mech. **116**, 77 (1959).

[30] B. E. Eaton, J. Fluid Mech. **180**, 117 (1987).

[31] V. A. Patel, J. Comput. Phys. **28**, 14 (1978).

[32] S. Taneda, J. Phys. Soc. Jpn. **11**, 302 (1956).